Journal of Cleaner Production 525 (2025) 146652

Contents lists available at ScienceDirect

Journal of Cleaner Production

journal homepage: www.elsevier.com/locate/jclepro

Characterizing the pore structure of wood materials: A conjoint analysis based on mercury intrusion porosimetry, N_2 adsorption and X-ray computed tomography methods

Zhipeng Zhu [a], Fan Wu [a], Xiaoxue Song [a], Wanli Cheng [a], Antoni Sanchez-Ferrer [b,*], Jingyao Zhao [a,**]

[a] Key Laboratory of Bio-based Material Science and Technology of the Ministry of Education, Northeast Forestry University, Harbin, 150040, China
[b] Wood Materials Science, Wood Research Institute of Munich (HFM), TUM School of Engineering and Design, Technical University of Munich, Winzererstr. 45, 80797, Munich, Germany

ARTICLE INFO

Keywords:
Wood materials
Pore size distribution
Pore structure
Mercury intrusion porosimetry
Nitrogen adsorption
X-ray computed tomography

ABSTRACT

Understanding the pore characteristics of wood is crucial for studying the micro- and macroscopic physical properties of this biomaterial and for predicting how effective any modification method would be. There is a need to better understand and determine the pore structure of wood materials. However, due to the wide pore size distribution (PSD) and its complexity, a single structural characterization method is usually insufficient for accurately interpreting the wood structure. In this study, the pore structure of wood is evaluated using a combination of X-ray computed tomography (XCT), nitrogen adsorption (N_2A), and mercury intrusion porosimetry (MIP), and the structural information is analyzed, compared and discussed in detail. Due to the voxel size of 2.00 μm^3 on the detection scale, the porosity measured by XCT was slightly lower than that obtained from MIP and N_2A - which can reach the nanometer detection level -, with N_2A being the method that yields the highest porosity. Although the PSD and the related parameters from the three methods differ, they are still capable of distinguishing between different wood species, and the average pore diameter and PSD obtained from the three different methods are similar, as well as the fractal dimension. Finally, the specific surface area values of the different wood species measured by N_2A range between 1 and 2 m^2/g. The combined characterization of numerous approaches, following their respective requirements, can provide a more comprehensive analysis of the intricate pore structure of wood materials.

1. Introduction

Wood is a natural organic nanocomposite material with distinct structural features, *i.e.*, complex and ordered structures, distinct hierarchy, and fine porous morphologies (Li Jian, 2021). Nanopores in the wood can be classified into macroscopic (>50 nm), mesoscopic (2–50 nm), and microscopic (<2 nm) pores at different scales. These pores primarily arise from the internal structural gaps in the cell wall and the rough surface of the structural elements, such as the vessel in hardwoods, the tracheid in softwoods, as well as fiber cells, resin channels and pits. The interconnected network formed by these elements serves as the main pathway for water migration and chemical penetration in wood (He et al., 2020; Yin et al., 2015, 2017), and plays a crucial role in the quality of wood after drying, impregnating and modification processes, influencing various properties such as density, dimensional stability, and mechanical strength of wood products (Fang et al., 2011; Papadopoulos et al., 2019; Redman et al., 2016; Yin et al., 2015). Moreover, the pore structure is a significant factor in determining the sound absorption, insulation properties, and humidity-conditioned performance of wooden products. The presence of such a continuous and interconnected internal gas network, together with the smaller and complex pore structures, contributes to enhanced sound absorption and insulation performance (Sánchez-Ferrer and Guerrero Parra, 2025). In humidity-conditioned wood products, the characteristics of the pore structures dictate the accessibility of water molecules, thereby influencing the capacity and efficiency of moisture absorption and release (El

---

* Corresponding author.
** Corresponding author.
E-mail addresses: sanchez@hfm.tum.de (A. Sanchez-Ferrer), zjy_20180328@nefu.edu.cn (J. Zhao).

https://doi.org/10.1016/j.jclepro.2025.146652
Received 13 May 2025; Received in revised form 20 August 2025; Accepted 13 September 2025

Assaad et al., 2023; Jang et al., 2020; Muthuraj et al., 2019; Sanchez-Ferrer et al., 2023; Zhang et al., 2024). Therefore, the study of the wood pore structures is essential for advancing wood processing techniques and improving the overall quality of wood products.

However, due to the complex structure and wide pore size distribution in wood, the evaluation of the pore structures has not been comprehensively and systematically explored for such a biomaterial. Currently, existing evaluation indexes for wood pore structures mainly include porosity, average pore size and pore size distribution, pore volume, specific surface area, and pore morphology, and techniques such as scanning electron microscopy (SEM), nitrogen adsorption (N_2A), mercury intrusion porosimetry (MIP), nuclear magnetic resonance (NMR), and X-ray computed tomography (XCT) hold significant potential for extracting information about wood pore structure (Burridge et al., 2021; Huang et al., 2025; Li et al., 2025; Xu et al., 2025; Yu et al., 2019; Zeng et al., 2023).

SEM is one of the most commonly used experimental methods for observing two-dimensional (2D) structures. However, this technique does not provide quantitative data in three dimensions (3D). Moreover, the porosity and pore size distribution obtained from SEM may be unrepresentative due to the complexity of the wood structure (Rajagopal et al., 2019). The MIP technique relies on the Washburn equation, establishing the relationship between pressure and pore size. Its detection range generally spans from 2 nm to 300 μm, even reaching up to 1000 μm (Michael and Niemz, 2011; Zhao et al., 2020). By assuming a pore network model, Portsmouth (Portsmouth and Gladden, 1991) extracted several characteristic parameters from MIP data curves through mechanistic analysis and numerical simulation to assess pore connectivity. The basic principle of N_2A involves the use of different models, such as the BET model for specific surface area and Kelvin's equation for pore size distribution, to establish the relationship between pressure and nitrogen adsorption capacity. This method can assess a narrow range of pore sizes, from approximately 0.35 nm–500 nm (Tibebu et al., 2023; Wang et al., 2020). In the 1990s, based on seepage theory, Seaton, Liu et al. conducted quantitative research on pore structure using various types of nitrogen adsorption hysteresis curves (N., 1991). Unfortunately, these fluid-based methods do not provide direct structural visualization and, thus, are considered indirect measurement techniques.

Since the 21st century, with the rapid development of imaging technology, 3D visualization of wood pore networks has become increasingly important. XCT is a radiation-based and non-destructive technique for visualizing the interior of canned objects, and for obtaining digital information on their 3D geometries and properties (Biziks et al., 2018; Hu et al., 2022; Taylor et al., 2013). As a strong contrast mainly exists between solid phases and air in foam materials, XCT can be applied to the study of porosity, and thus to wood characterization. The pore size detection range is generally between meso- and macroporosity. Using XCT technology, Brodersen et al. reconstructed the conduit network of *Vitis vinifera* and analyzed its connectivity and distribution characteristics (Brodersen et al., 2013). By further improving resolution, Trtik et al. captured the location and 3D structure of softwood pits (Trtik et al., 2007). Wason et al. conducted a detailed study on the morphological characteristics of vessel ends and the connectivity between the annual rings of hardwood (Wason et al., 2019). However, due to resolution limitations, the porosity detected by this method is usually lower. In addition, calculations based on XCT data typically employ a ball-and-stick model for pore size analysis, which is obviously not consistent with the actual wood structure. Therefore, these points need to be further studied.

Despite significant progress in various numerical and experimental techniques for characterizing wood pore structures, there are only a few studies in the literature that address the differences and similarities in the results obtained from different techniques, such as MIP, N_2A, and XCT (Razavifar et al., 2021; Zhang et al., 2022). Additionally, comprehensive comparisons of the results obtained from these techniques and their respective scopes of application are rare. Furthermore, these state-of-the-art techniques suffer from technical limitations and shortcomings in the conceptual models commonly used to interpret their results.

Thus, to overcome the limitations identified in current literature, we employed a multi-technique characterization approach, i.e., MIP, N_2A, and XCT, to examine the pore structure properties of sapwood samples from Mongolian Scots pine, Asian birch, and Mongolian oak. Key pore structural parameters, including porosity, average pore size, pore size distribution, and fractal dimension, were systematically compared and analyzed. The results from this study demonstrate that these three methods are complementary in different pore size ranges, and their combined application can provide more comprehensive information on the different wood pore structures. By establishing robust structure-property relationships, this synergistic approach enables more accurate predictions of performance for critical wood processing stages, such as drying kinetics, modification efficiency, and dimensional stability. The quantified pore network parameters directly address longstanding industrial challenges, such as uneven penetration of wood preservatives and inconsistent resin distribution in engineered wood products. Additionally, this methodology provides data-driven insights for optimizing industrial workflows - from preservative impregnation protocols to adhesive application parameters - thereby improving process efficiency, reducing energy consumption, and minimizing material waste.

2. Materials and methods

2.1. Materials preparation

This study selected three types of wood based on the GB/T 1927.1, 2–2021 standards, namely Scots pine (*Pinus sylvestris*, a coniferous wood), White birch (*Betula platyphylla*, a diffuse-porous deciduous wood) and Mongolian oak (*Quercus mongolica*, a ring-porous deciduous wood). The air-dried densities of these species were 527 ± 22, 587 ± 14, 659 ± 22 (mean ± standard deviation), respectively - obtained with an X-ray densitometer (DPX300-LTE). To minimize the changes in test results caused by sample differences, the same specimen for each wood species was used for all three tests, and based on the characteristics of the detection methods, the testing sequence was as follows: XCT (non-destructive sample), N_2A (recoverable sample), and MIP (contaminated and non-recyclable samples). The sample dimensions were of a cylindrical sapwood specimen of 2 mm in diameter and 2 mm in height. Each sample contains an entire annual ring with both early wood and late wood. Firstly, before conducting the XCT test, the surface of the samples was polished with 1000-grit sandpaper, and any wood dust was removed. Samples were dried in an oven at 103 °C, after which it was tightly wrapped in silica gel to prevent changes in moisture content. Due to the particularity of N_2A and MIP detection, a $1 \times 1 \times 2\ \text{mm}^3$ square prism with a weight of approximately 0.2 g was cut from the center of the sample using a blade after the XCT experiment was performed. To ensure the reliability of the data, each test for each wood species was repeated twice. The whole analysis procedure is shown in Fig. 1.

2.2. X-ray computed tomography (XCT) experiments

XCT experiments were performed using a Nano Voxel 3000 system (Tianjin Sanying Precision Instruments Co., Ltd.). The maximum sweep voltage and current were 100 kV and 200 μA, respectively. The resolution was less than 5 μm, with the detector having a minimum of 4800 × 3200 physical pixel units. The maximum resolution of a single two-dimensional reconstructed slice was at least 12000 × 12000 pixels. The rotary scanning mode was used with a single image exposure time of approximately 1500 ms, and 90 min were required to complete the scan on the cylindrical wood sample. A Dell Precision 7530 workstation was used for processing the data, saving the data in 16-bit raw format, with the original data size of 1000 × 1000 × 1000 voxels of an approximate

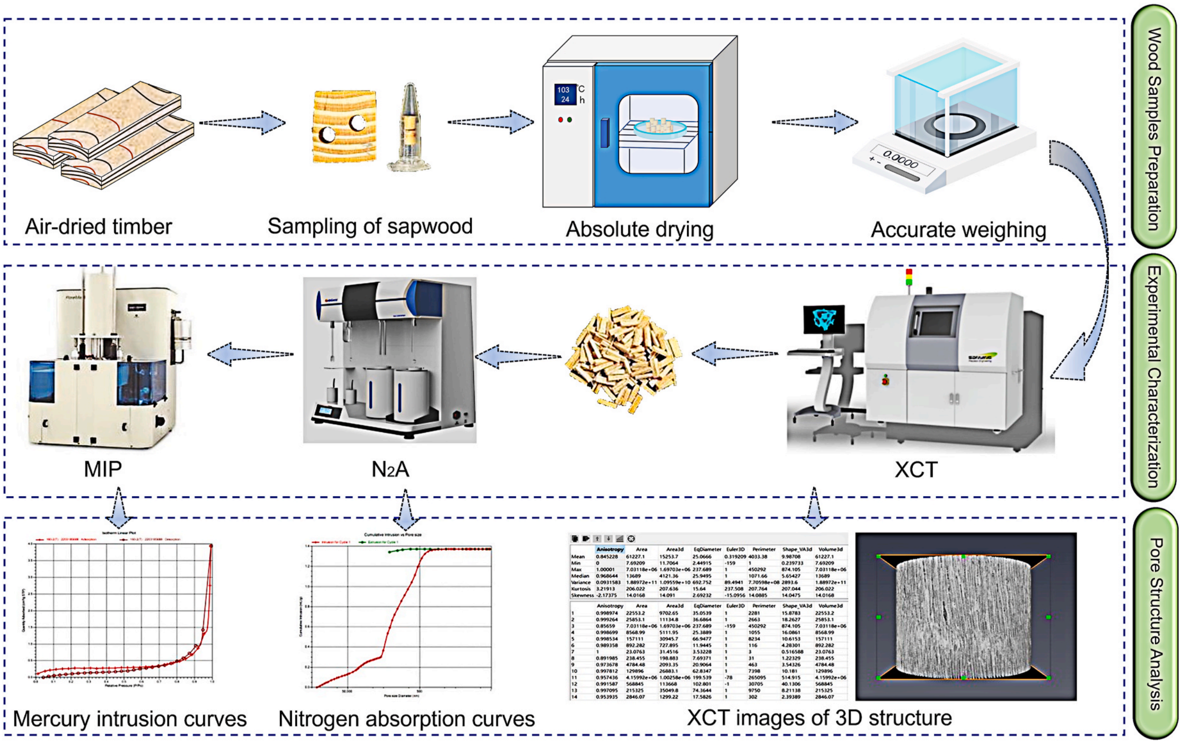

Fig. 1. Wood samples preparation, experimental characterization and pore structure analysis.

size of 2.00 μm^3 per voxel. The image data obtained from each XCT scan were digitalized before proceeding with image recognition and quantitative analysis. The overall analysis included slice imaging, volume rendering, image cropping, noise filtering, threshold segmentation, marking, quantitative evaluation, and seepage simulation. All these operations were performed using the Avizo 9.0.1 and ImageJ 1.52a 3D visualization software packages (Wildenschild and Sheppard, 2013).

2.3. Nitrogen adsorption (N_2A) experiments

N_2A experiments were performed using an ASAP 2460 instrument (Micromeritics Instrument Corporation, USA) to obtain information on specific surface area, pore volume, and pore size distribution. Each sample was placed into a sample cell and outgassed at 80 °C for 10 h under high vacuum ($<10^{-5}$ Pa) to remove bound moisture and adsorbed contaminants from the sample surface. Nitrogen and helium were used as the adsorption and carrier gas, respectively, and introduced into the material in a specific proportion. The pore volume was determined using nitrogen adsorption isotherms from the amount of nitrogen adsorbed at a relative pressure close to unity. The pore shape was calculated based on the hysteresis loops. The specific surface area was calculated using the Brunauer–Emmett–Teller (BET) equation, and the pore size distribution was derived using the density functional theory (DFT) following the international standard ISO-15901. Since the nitrogen adsorption method cannot determine porosity, a gas expansion porosimeter (VINCI, France) was used to measure the porosity of the samples (Mohammadi et al., 2020) based on Boyle's law for gases.

2.4. Mercury intrusion porosimetry (MIP) experiments

MIP experiments were carried out in an AutoPore IV 9500 mercury porosimeter (Micromeritics Instrument Corporation, USA) to assess the pore volume, porosity, and pore size distribution. The oven-dry samples were placed within a sealed chamber to ensure isolation from the environment. The measurement began with a gradual increase in pressure, ranging from 0.1 psia to 60, 000 psia (689 Pa–414 MPa), while the sample was submerged in non-wetting mercury. Each pressure increment had a 10 s equilibrium time to ensure accuracy. The instrument automatically adjusted the pressure increase rate, slowing it at lower pressures for better precision. As the pressure increased, mercury progressively infiltrated the sample, moving from larger to smaller voids, thus allowing for a comprehensive analysis of the wood's internal structure. Each scan cycle lasted approximately 60 min, during which the amount of intruded mercury was recorded. After scanning, the pore volume was calculated based on the volume of mercury that penetrated the samples. The pore size distribution was subsequently determined using the Washburn equation. The pressure increase rate was automatically adjusted by the advanced control system of the instrument, which employed slower rates at lower pressure levels to enhance precision during the mercury intrusion. As the pressure increased, mercury progressively infiltrated the sample, moving from larger voids to smaller ones, thus allowing for a comprehensive analysis of the wood's internal structure. Each scan cycle lasted approximately 60 min, during which the amount of intruded mercury was recorded. After completing the scans, the pore volume was calculated based on the volume of mercury that penetrated the samples. The pore size distribution was subsequently determined using the Washburn equation (Zhao et al., 2020).

2.5. Scanning electron microscope (SEM) experiments and vertical density profile (VDP) experiments

The cross-section of the wood samples was examined using a scanning electron microscope (EVO18, Carl Zeiss, Germany) with a secondary electron detector at 5–10 kV. The vertical density profile (VDP) of the wood specimens with dimensions 50 mm × 50 mm × 25 mm (L × T × R) was determined using an X-ray densitometer (DPX300-LTE) following the LY/T 2718-2016 standard. Density measurements were taken at 0.05 mm intervals across the thickness of the specimens.

3. Results and discussions

3.1. Pore structure analysis based on XCT experiments

From the XCT scan images (Fig. 2), the internal structure of the wood from different axes, *i.e.*, transverse, tangential, and radial directions (L, T, R), is shown, with black representing pores and gray representing the matrix. The voxel dimensions for the three wood species were 1.906, 1.934, and 1.996 μm^3, respectively. Based on the voxel values, it can be inferred that these experiments are only capable of detecting pores with a minimum size of approximately 2 μm. Within this size range, the tracheid, resin canals, and wood rays of softwood were visible, as well as the vessels, wood fibers, wood rays, and tyloses of hardwood. Although microscopic imaging clearly revealed the presence of pores on cell walls (Fig. 2g–i), their diameters (from 0.8 to 20 μm) partially exceed the resolution limit of XCT. Consequently, some of the pores may not be identifiable. According to the International Chemical Organization's standards, the pores detected in this study fall within the macropore range (>50 nm). XCT technology not only excels in structural visualization but also offers distinct advantages in the quantification of structural parameters. As it is well known, the quantitative analysis of structural parameters is crucial for the numerical simulation of material reconstruction and property prediction. Therefore, based on the XCT structural visualization, key structural parameters such as porosity (volume/surface), pore size distribution, fractal dimension, and anisotropy index were evaluated.

As shown in Fig. 3, the porosity distribution and fractal dimension along different sections along the L-axis - transverse direction - for the three wood species are presented. The results showed that the porosity and fractal dimension for the different slices were not constant within the sample's slices but exhibited a fluctuating, random distribution. The average porosity values (mean ± standard deviation) for the three wood species and the minimum and maximum values – in parentheses - were 0.580 ± 0.005 (0.570–0.592), 0.468 ± 0.003 (0.462–0.476), and 0.377 ± 0.004 (0.366–0.386), respectively, which are inversely proportional to the corresponding wood densities. Nevertheless, these values can be considered quite accurate since the standard deviation values account for *ca.* 1 % of the corresponding mean value. Neither the tracheid of softwood nor the vessels of hardwood show cylindrical pore cross-sectional shape with uniform longitudinal pore sizes as shown in

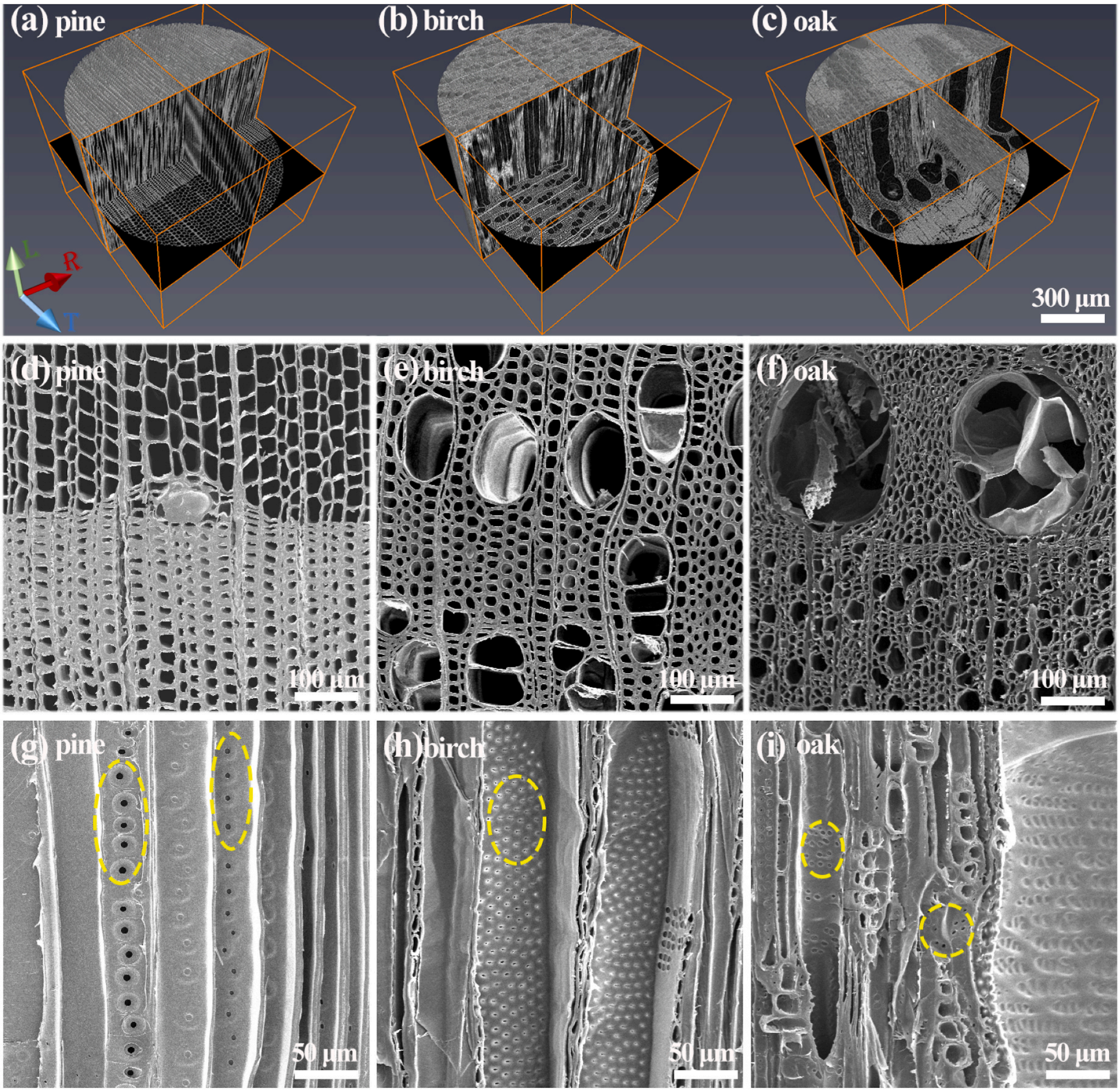

Fig. 2. 3D XCT scan images for a) pine, b) birch, and c) oak, and the corresponding SEM images of cross section d), e) and f), and tangential section g), h) and i) of three wood species, respectively (The pits are marked by yellow dotted lines). (For interpretation of the references to colour in this figure legend, the reader is referred to the Web version of this article.)

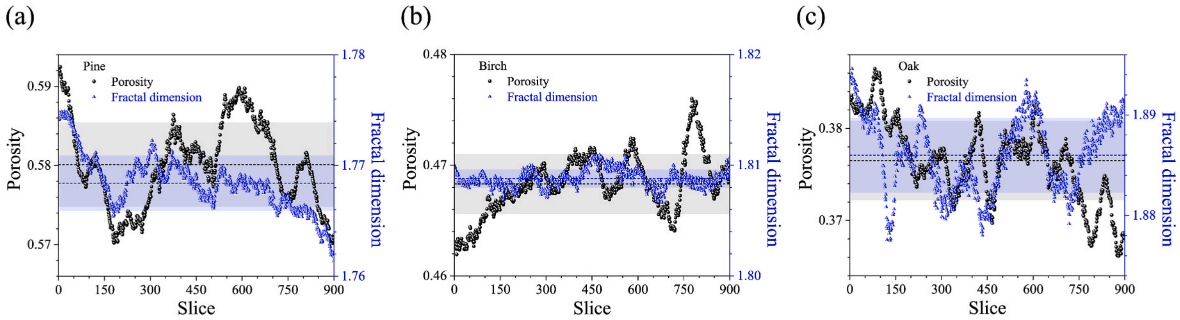

Fig. 3. Porosity values and fractal dimension of (a) pine, (b) birch, and (c) oak obtained from different slices out of the XCT experiments along the L-direction. The lines are the mean values and the areas correspond to 2 sigma values.

Fig. 2. Therefore, it was inevitable that the pore size and distribution vary across layers, resulting in the porosity distribution in Fig. 4. The fractal dimension distribution followed a similar trend due to the variation in pore arrangement and size across different slices. The average fractal dimensions for the three species were 1.768 ± 0.003 (1.761–1.775), 1.809 ± 0.001 (1.807–1.811), and 1.886 ± 0.004 (1.878–1.895), respectively.

To further investigate the relationship between porosity and fractal dimension, a correlation analysis was conducted. It was found that pine exhibited a moderate correlation ($R^2 = 0.69$), while the correlation for birch and oak was very weak ($R^2 = 0.27$ and 0.34, respectively). Previous studies, such as Zhao et al. (2023), suggested a correlation between porosity and fractal dimension. Generally, the fractal dimension can characterize the complexity of the pore structure. Materials with high porosity tend to offer relatively large pore volumes and numbers, offering more options for varied pore arrangement and distribution. As a coniferous wood, pine has a simple pore structure from the tracheids, resin channels, parenchymas, rays and pits. In contrast, birch and oak - both hardwoods -, have a more complex pore structure that includes vessels, fibers, parenchyma, rays and pits in a diffuse-porous and ring-porous fashion, respectively. The relationship between porosity and fractal dimension is also influenced by the arrangement of the pores, making the correlation extremely variable.

The pore size distribution (PSD) is another important parameter for evaluating the pore structures. However, due to the complexity of wood and the limitations of the analytical techniques, obtaining accurate PSDs is very challenging. Calculations based on XCT data typically used a ball-and-stick model for the pore size analysis, which did not accurately reflect the actual wood structure. Therefore, in this study, a layered pore size calculation method was employed, where the PSD was determined by analyzing the PSD of each slice. The PSD has generally been expressed as a density distribution. Table 1 shows the PSD for the three wood species, and the average pore diameters for pine, birch, and oak were 18 (PI = 1.1; range: 8–79 μm), 16 (PI = 2.1; range: 4–164 μm), and 28 (PI = 3.1; range: 13–314 μm) μm, respectively – PI is the polydispersity value. Additionally, it can be observed that the PSDs of the three wood species follow a normal distribution, with $\mu \pm \sigma$ values of 18 ± 4, 15 ± 4 and 26 ± 12 μm for pine, birch and oak, respectively. The main reason for this variation was related to the wood structure. For instance, pine (softwood) is primarily composed of tracheids, which have relatively consistent pore sizes along the L-direction and are larger than fibers in hardwoods, but vary between earlywood (14 μm) and latewood (4 μm) and contain sporadic resin channels. In contrast, birch and oak (hardwoods) contain both small-pored wood fibers (5–13 μm and 3–9 μm, respectively) and large vessels (50–150 μm and 205–350 μm, respectively), resulting in a broader PSD (*i.e.*, PI = 2.1 and 3.1, respectively).

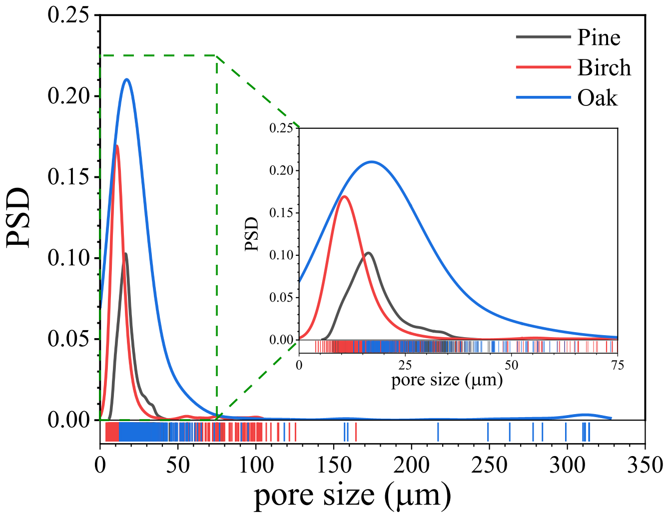

Fig. 4. Pore size distributions (PSD) obtained from the XCT experiments for the three wood species.

Based on the above structural parameters, the basic pore structure parameters for different wood species are provided in Table 1, together with the permeability parameter that can be directly simulated using XCT technology. From this data, the anisotropy index A to assess the structural anisotropy was calculated as $A = K_{min}/\sqrt{K_{med}K_{max}}$, where $K_{\min}$, K_{med} and $K_{\max}$ represent the minimum, median, and maximum permeability, respectively (Zhao et al., 2023). From Tables 1 and it was evident that the axial permeability of the three species was significantly higher than their radial and tangential permeabilities, with little difference between radial and tangential permeability. This was related to the wood structure, as wood has good axial connectivity. The permeability and porosity of the three wood species were closely related (Zhao et al., 2023). The anisotropy index of oak was significantly higher than that of the other two wood species, which was closely linked to its structure. From a structural perspective (Fig. 2), the pore size and pore size distribution for oak are highly irregular, resulting in a considerable difference in the anisotropic properties. Additionally, the anisotropy index correlates with the fractal dimension, as both parameters tend to increase as porosity decreases.

The axial connectivity of the wood porous structure has been analyzed by assessing the ratio of the total connected volume to the total volume of the wood sample. As shown in the connected structure data in Table 1 and Fig. 2, wood's connectivity is relatively low and could be affected by factors such as the selection of the sample and the calculation method used. If the selected sample contains an intact conduit (tracheid, vessel or wood fiber), the connectivity results in a higher value. Connectivity is a topological property that indicates an uninterrupted pathway system; however, in the wood porous structures studied, fully connected pores extending through an entire sample are rare; most pores are only partially connected (Zhao et al., 2020). The pits on the cell walls were distinctly visible in Fig. 2 and serve as conduits for lateral

Table 1

Structural parameters, *e.g.*, total void volume (V_p), porosity (ϕ), minimum, maximum and average pore size ($r_{\min}$, $r_{\max}$ and r_{avg}), fractal dimension (D_f), connectivity (C), permeability (K) and anisotropy (A) obtained from the XCT analysis.

Samples	V_p (mm^3)	ϕ	$r_{\min}$ (μm)	$r_{\max}$ (μm)	r_{avg} (PI) (μm)	D_f	C (%)	K $[L/R/T]$ (mD)	A (%)
Pine	3.64	0.580	8	79	18 (1.1)	1.768	1.31	28.63/0.34/0.79	1.737
Birch	2.88	0.468	4	164	16 (2.1)	1.808	3.51	13.56/0.09/0.13	2.501
Oak	2.36	0.376	13	314	28 (3.1)	1.886	5.38	1.44/0.23/0.45	19.123

connectivity within the wood tracheids (pine) and vessels (birch and oak). These structures exhibited diameters ranging from 0.8 to 20 μm, with some exceeding the resolution limit of XCT. The diameter of the pits in coniferous wood was slightly larger than that in deciduous wood. Due to the simpler anatomical organization of coniferous wood, pit connectivity represents the primary pathway for lateral transport. Therefore, accurate characterization of pit morphology and distribution in coniferous species became particularly crucial for reliable connectivity assessment. The connectivity values through XCT were likely underestimated due to the inherent technical limitation of this method.

3.2. *Pore structure analysis based on N_2A experiments*

Fig. 5 shows the nitrogen sorption isotherms for the three different wood species. The relative pressure range was between 0.001 and 0.995, with a total adsorption capacity of approximately 2.8 cm^3/g. According to the IUPAC adsorption isotherm classification, the adsorption curves of the different wood species fall into a mixed type II and IV category. These isotherms are characterized by a rapid increase in the adsorption capacity at low relative pressures (approximately 0.2). In this stage, single-layer adsorption predominantly occurred. When the relative pressure exceeds 0.2, the nitrogen adsorption increases less as the relative pressure rises, with multi-layer adsorption occurring during this phase. When surpassing 0.8 relative pressure, nitrogen adsorption increases abruptly again due to capillary condensation, where a large number of nitrogen molecules turn into liquid and fill the pores of the wood. Once adsorption was completed, desorption curves were measured. Theoretically, the desorption curve should coincide with the adsorption curve. However, in practice, there were some differences, which can be categorized into four types (Yin et al., 2015, 2017). The absorption and desorption curves in this study showed a significant deviation from the expected type, indicating that the pore structure of wood was highly complex, and the pore types were likely a mixture of several pore types. The resulting hysteresis indicated that the pore structure was primarily splinted and existed mainly in the cell wall pores and the microfibril interstices. Similar curve shapes have been reported in previous studies of western red cedar heartwood, Douglas-fir heartwood, and aspen heartwood (Wanwan et al., 2022).

A careful observation of these curves revealed that the adsorption and desorption isotherms did not coincide and exhibited a crossover, which differs from the previous experimental results (Tibebu et al., 2023). The adsorption-desorption behavior of wood exhibited significant hysteresis phenomena attributable to its unique structural and morphological characteristics. The combination of relatively low specific surface area and complex hierarchical pore architecture induces pronounced pore resistance and ink-bottle effects, creating fundamentally divergent adsorption and desorption pathways. Particularly in the intermediate pressure range, certain mesopores demonstrate higher desorption efficiency than their corresponding adsorption efficiency, resulting in a characteristic curve crossing. This behavior may be further exacerbated by incomplete sample degassing due to the inherent limitations of conventional degassing methods in completely removing residual extractives and moisture trapped within the micro/nanostructure of the wood. These observations were consistent with some previous studies, which underscored the challenges in accurately characterizing wood's pore structure (Mo et al., 2022; Tibebu et al., 2023). To eliminate the influence of these factors, some researchers (Yin et al., 2015) have applied powder treatment and supercritical drying to the material. The powder treatment broke the wood's microstructure, thereby increasing the specific surface area, while supercritical drying more effectively removes adsorbed gases. However, this study did not adopt these methods because the powder treatment compromised the wood's true pore structure, and the increased specific surface area is not representative of the wood's original structural characteristics, and supercritical drying is not a conventional technique and is ineffective for large, bulky objects.

The specific surface area and pore size distribution were calculated using the corresponding models based on the adsorption and desorption curves. In this study, the BET and BJH models were applied to calculate the pore size distribution and specific surface area. From Fig. 6, the mesoporous pore size distribution of the three wood species appeared very similar, with the maximum pore size around 15 nm and average values of 16 (PI = 3.2; range: 1.7–176 nm), 11 (PI = 2.6; range: 3.7–156 nm) and 16 (PI = 2.3; range: 1.9–184 nm) nm for pine, birch and oak, respectively – in parenthesis the polydispersity for each pore size distribution (Table 2). The surface area values of the three species were 1.689, 1.538 and 0.985 m^2/g for pine, birch and oak, respectively. According to adsorption theory, the specific surface area is primarily determined by mesoporous pores. Hence, the specific surface area of wood was relatively smaller due to the lower mesoporous content.

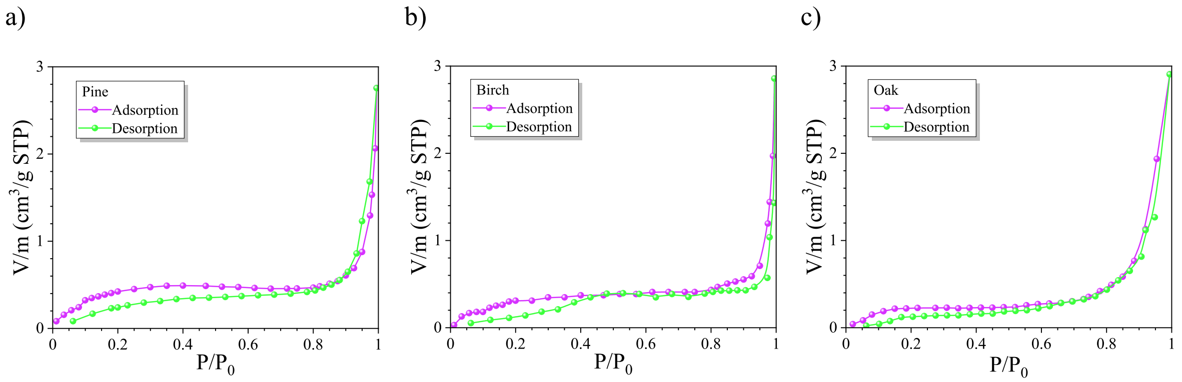

Fig. 5. Nitrogen adsorption and desorption isotherms for (a) pine, (b) birch and (c) oak.

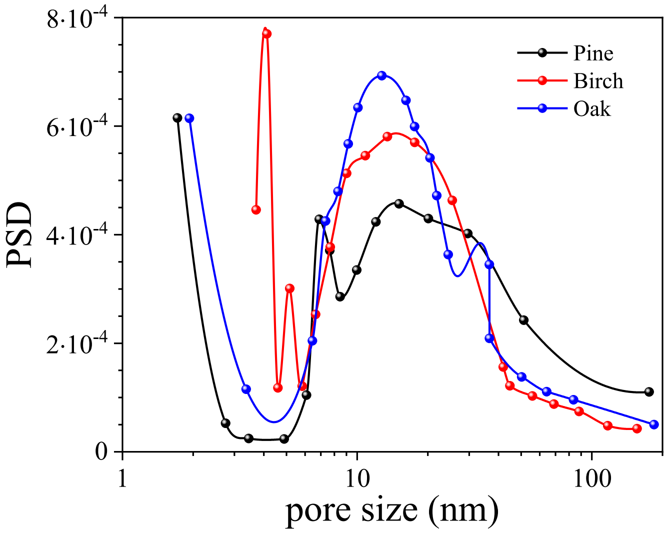

Fig. 6. Pore size distribution (PSD) obtained from the N_2A experiments for the three wood species.

For wood, such pores are mainly located in the cell wall and the microfibril gap, which have a larger specific surface area and strong adsorption capacity. The differences in the mesoporous range and the mean values of the three species were minimal, indicating that the mesoporous characteristics of the wood were not significantly different. Generally, large pores only serve as channels for gas adsorption, while small pores are too narrow for nitrogen molecules to enter. Additionally, these pores do not easily establish an adsorption relationship with the gas due to the influence of van der Waals forces. Therefore, it can be concluded that the nitrogen adsorption method is not effective for determining the porosity of the wooden material. As a result, in this study, the porosity was measured using Boyle's law, and the fractal dimension was determined by the FHH method (Li et al., 2018). From Tables 2 and it was evident that, except for porosity, the nitrogen adsorption data for different wood species were very similar, suggesting that the mesoporous structure of these species was essentially the same. This finding was consistent with results from Tibebu et al. (2023).

3.3. *Pore structure analysis based on MIP experiments*

The mercury intrusion porosimetry (MIP) curves of the three wood samples are shown in Fig. 7a–c, which include both the cumulative intrusion and extrusion curves. As shown in Fig. 7a–c, when the pressure reached 40,000 psia, the mercury injection process for all three samples had essentially concluded. However, to avoid missing any macroporous structures, tests were conducted within the pressure range of 0.1–60,000 psia, where the former value was not the pressure at which mercury first entered the sample chamber. As the intrusion pressure increased, mercury was initially forced into the larger pores at lower pressures, followed by into the smaller pores at higher pressure values. The cumulative mercury intrusion uptake increased accordingly, with the extent of the uptake being structure-dependent. For the three wood species, *i.e.*, pine, birch and oak, the intrusion pressure started at a threshold value of *ca.* 0.5 psia. At this point, pine showed two regions

Table 2

Structural parameters, *e.g.*, total nitrogen volume per mass (V_{N2}), porosity (ϕ), minimum, maximum and average pore size ($r_{\min}$, $r_{\max}$ and r_{avg}), fractal dimension (D_f), specific surface area (S_{BET}), and BET average pore size (r_{BET}) from the N_2A experiments for the three wood species.

Samples	V_{N2} (cm^3/g)	ϕ	$r_{\min}$ (nm)	$r_{\max}$ (nm)	r_{avg} (*PI*) (nm)	D_f	S_{BET} (m^2/g)	r_{BET} (nm)
Pine	2.756	0.673	1.7	176	16 (3.2)	1.801	1.689	9
Birch	2.857	0.591	3.7	156	11 (2.6)	1.798	1.538	10
Oak	2.905	0.493	1.9	184	16 (2.3)	1.752	0.985	12

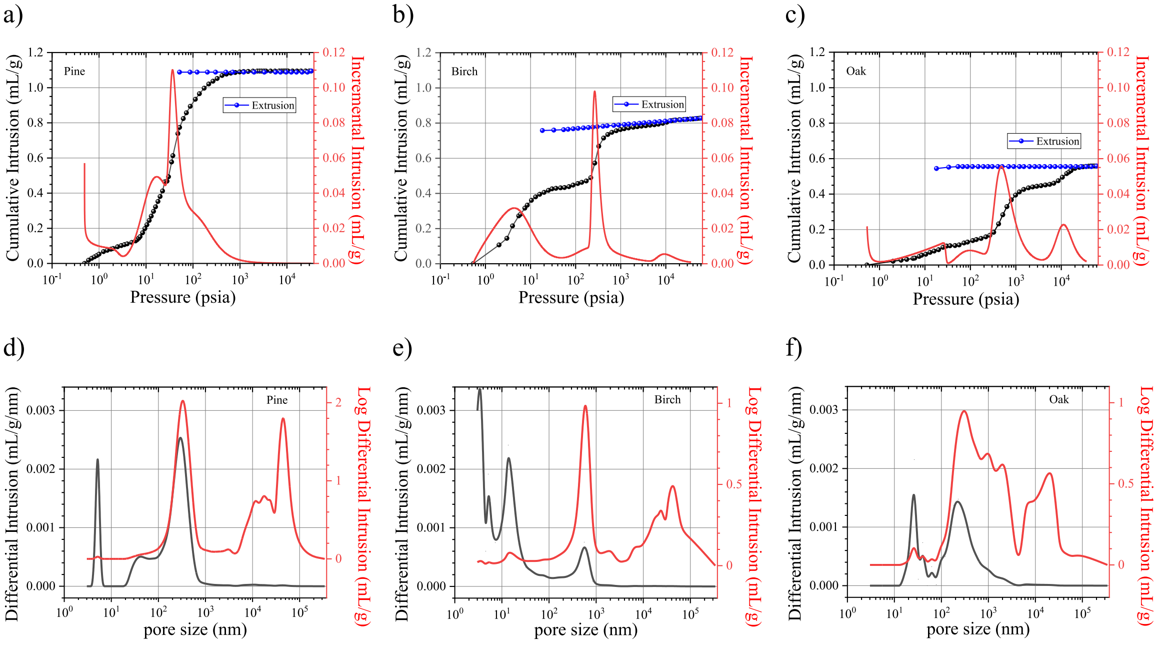

Fig. 7. Cumulative and incremental mercury intrusion curves for (a) pine, (b) birch and (c) oak, and differential and log differential mercury intrusion pore size distributions for (d) pine, (e) birch and (f) oak.

with a local maximum in the incremental mercury intrusion profile, *i.e.*, at 17 psia (from 3.5 to 25 psia) and 37 psia (from 25 to 33000 psia). Both hardwoods – birch and oak - presented three local maxima at 4.5 psia (from 0.5 to 50 psia), 265 psia (from 50 to 4450 psia) and 9500 psia (from 4450 to 36000 psia); at 99 psia (from 0.5 to 200 psia), 480 psia (from 200 to 3750 psia) and 11200 psia (from 3750 to 36000 psia), respectively. These steps correspond to the different sizes in the pore population, where low pressures are related to big pore sizes and vice versa.

To obtain the PSD, the differential and log differential mercury intrusion profiles were calculated. Fig. 7d–f illustrates the pore size distribution for the three wood samples. In the differential intrusion profiles, two peaks below 30 nm at between 250 and 600 nm were observed. In contrast, the log differential intrusion profiles show two peaks: one between 250 and 600 nm and the second one between 20 and 50 μm. Thus, from the differential and log differential mercury intrusion curves, three distinct pore size groups were identified: larger macropores (from 1-5 μm–350 μm), macropores (from 50-100 nm to 1–5 μm), and mesopores (up to 50–100 nm).

The pore structural parameters of the three wood species are summarized in Table 3. In addition to basic parameters, several characteristic parameters were also determined. For instance, the threshold pressure (P_t) represents the point when mercury first intrudes into the pores of the sample, providing an initial indication of the pore size; it is not the pressure at which mercury first enters the sample chamber. Generally, the lower the threshold pressure, the easier it is for mercury to enter the pores. As shown in Table 3, a low threshold pressure of 0.49 psia was associated with a higher mercury uptake per unit mass (1.089 mL/g), suggesting a larger pore size (367.8 μm). Tortuosity (τ) is a key quantitative indicator used to describe the difficulty of fluid diffusion through the material and plays a crucial role in distinguishing between free and forced fluid flow (Yuan et al., 2016; Yun et al., 2010). In this study, tortuosity ranged from 1.9 to 6.2, and from these values, oak seems to be the wood species with higher tortuosity, followed by birch and, finally, pine. The fractal dimension (D_f) is another parameter used to characterize the complexity of the material's structure, with values for the three species being approximately 1.7. However, the accuracy of these characteristic parameters heavily depends on the calculation method.

3.4. Comparison of the results from the three methods

In order to get a better picture of each technique and to compare the pore size scales for each method, the corresponding PSD curves are shown in Fig. 8. The MIP PSD curves clearly indicate the presence of three distributions corresponding to the meso-, macro- and large macropores, while the N_2A and XCT PSD curves mainly show in the mesoporous and the marge macroporous regions and data in the macroporous region is missing or incomplete. Therefore, MIP experiments show a more complete picture of the pore size regions in wood materials, and N_2A and XCT experiments are complementary to the former. The comparative analysis of the three methods revealed distinct species-dependent pore structures in wood species. N_2A analysis indicated minimal interspecies variation in mesoporous characteristics, with differences of less than 5 nm in average pore size (Table 2), suggesting nearly identical mesopore-related transport properties across species. However, significant variations emerge in macroporous structures. Softwood exhibited a narrow pore size distribution in XCT analysis, consistent with its homogeneous tracheid-based anatomy, while ring-porous hardwood (oak) showed a broad distribution reflecting its heterogeneous tissue composition containing vessels, fibers, and parenchyma. This structural complexity in hardwoods also manifested as higher MIP curvature values, indicating greater pore network tortuosity compared to the more uniform softwood structure of pine. These findings demonstrated that while mesoporous features remain similar across species, macroporous architecture varies substantially according to wood anatomical classification.

Fig. 9 shows the comparison of porosity, fractal dimension, average pore size, and permeability values obtained by the three methods, clearly highlighting the differences in data derived from each technique. This phenomenon was consistent with our expectations due to the differences in the principles and scales of the detection methods. However, except for the fractal dimension, the other parameters provided consistent results for evaluating the three wood species. Specifically, the porosity followed the order: pine > birch > oak – which is inversely proportional to the corresponding density. The porosity value measured by XCT was smaller than that obtained by MIP, and this was smaller than that measured by N_2A, likely due to the detection method. In the N_2A analysis, macropores primarily function as gas transport channels, while micropores remain inaccessible to nitrogen molecules due to kinetic diameter restrictions. Additionally, weak van der Waals interactions further limit gas adsorption in these confined spaces. Consequently, N_2A measurements effectively characterize the mesoporous structure (2–50 nm). MIP employs high-pressure mercury penetration to evaluate porosity and pore size distribution based on the Washburn equation, predominantly detecting macropores (>50 nm). In contrast, XCT exhibits a resolution limit of approximately 2 μm, rendering it insensitive to finer pore structures. These methodological differences explain the systematically higher porosity values obtained from N_2A compared to MIP and XCT measurements. Moreover, during the nitrogen filling process, capillary condensation may have occurred, leading to an excessive number of nitrogen molecules entering the wood pores and also resulting in a higher measured porosity.

The pore architecture characteristics quantified through MIP, N_2A, and XCT critically determine the macroscopic properties of wood. N_2A analysis revealed that mesopore distribution (2–50 nm) predominantly regulates hygroscopic behavior, where the mesopore volume of birch correlates with increased moisture adsorption capacity due to stronger capillary forces. In contrast, the large macropores' dominance of pine facilitated fast moisture transport but diminished retention capacity. Mechanical performance demonstrated an inverse porosity dependence (pine > birch > oak), with oak's well load-bearing capacity deriving from its lower porosity and higher density (659 kg/m^3). XCT connectivity analysis elucidated oak's better dimensional stability, showing how its tortuous, low-connectivity pore pathways effectively retard moisture diffusion. Conversely, pine's highly interconnected macroporous network compromises transverse strength through reduced interfiber bonding. These structure-property relationships enable performance-optimized material selection for specific applications. Future research should focus on integrating multiscale pore network data with standardized mechanical and hygroscopic testing protocols to establish predictive performance models that account for anatomical

Table 3

Structural parameters, *e.g.*, total mercury volume per mass (V_{Hg}), porosity (ϕ), average meso-, macro-, and large macropore size (r_{meso}, r_{macro} and r_{MACRO}), average pore size (r_{avg}), fractal dimension (D_f), tortuosity (τ), permeability (K) and threshold pressure (P_t) obtained from the MIP analysis for the three wood species.

Samples	V_{Hg} (cm^3/g)	ϕ	r_{meso} (nm)	r_{macro} (nm)	r_{MACRO} (μm)	r_{avg} (*PI*) (μm)	D_f	τ	K (mD)	P_t (psia)
Pine	1.089	0.648	5 (1.0)	334 (1.2)	27 (1.4)	14 (2.7)	1.718	1.9	70.597	0.49
Birch	0.756	0.545	10 (2.5)	669 (1.5)	31 (1.4)	14 (3.2)	1.703	3.4	62.466	0.54
Oak	0.544	0.443	31 (1.1)	895 (1.9)	18 (1.5)	6 (4.3)	1.672	6.2	31.832	0.53

Note: the polydispersity values for each average pore size values are in parentheses.

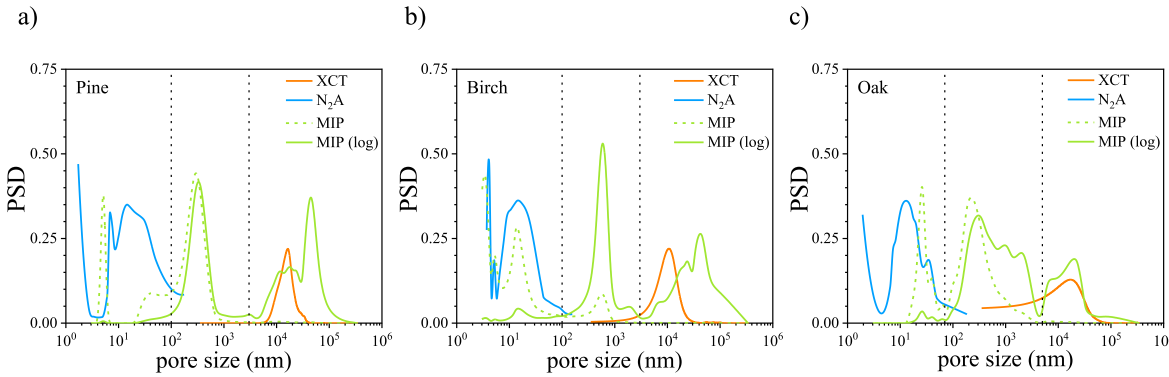

Fig. 8. Normalized pore size distribution (PSD) functions for a) pine, b) birch and c) oak, from XCT (orange), N_2A (blue) and MIP (green) experiments. (For interpretation of the references to colour in this figure legend, the reader is referred to the Web version of this article.)

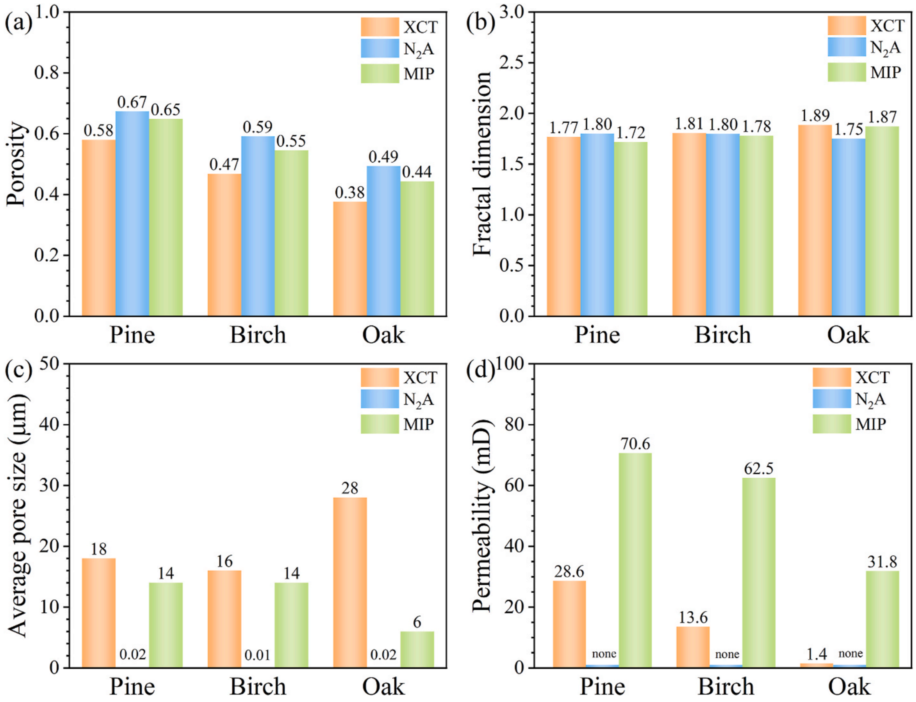

Fig. 9. Comparison of the results obtained from the different methods, *i.e.*, XCT, N_2A and MIP for the three wood species: (a) porosity, (b) fractal dimension, (c) average pore size, and (d) permeability.

variations across species.

The average pore size values revealed that the results from XCT were similar to those from MIP, and both fell within the macropore range. In contrast, N_2A, due to its different detection principle, measured pore size values within the mesopore range. The fractal dimension values are quite consistent between the three methods, ranging from 1.7 to 1.9. Currently, the calculation methods for fractal dimension rely on different models, which inevitably lead to discrepancies in the outcomes. The permeability values revealed substantial differences between transverse and axial permeability measured by XCT. It was observed that the results from MIP were significantly higher than the XCT results. This discrepancy may be related to the pressure applied during the MIP test. In the MIP mercury intrusion process, mercury enters the wood from three directions, and the increased number of flow paths naturally leads to higher permeability. Furthermore, the increased pressure during the test likely caused micro-cracks in the wood structure, which further contributed to the observed increase in permeability.

To account for differences in the methods used to evaluate the PSD and eliminate unit discrepancies, the distribution was normalized, with the pore size proportion constrained between 0 and 1. Excluding variations in wood structure, the PSD results are satisfactory, indicating consistency in the data obtained from all three methods. Any observed differences can be primarily attributed to structural variations and the distinct principles underlying each detection method. Furthermore, noticeable peaks appeared at each scale based on the detection scales of the different methods, suggesting that the three approaches were complementary. For example, N_2A and XCT address the limitations of MIP in detecting mesopores and larger macropores, respectively. The PSD range detected by N_2A and XCT was relatively narrow. As mentioned earlier, each detection method was based on different principles and operates at different scales, providing unique structural characterization data. Therefore, joint characterization allowed for the analysis and quantification of pore structure characteristics from various perspectives. For instance, XCT radiation technology offered clear advantages in computational connectivity, anisotropy, and simulation, providing not only a visual representation of the structure but also the ability to calculate macroscopic properties. MIP and N_2A fluid technologies are indirect detection methods; they could offer valuable structural information at their respective scales, such as specific surface area, fractal dimension, and tortuosity, when combined with appropriate geometric models.

Consequently, the development of pore structure characteristic parameters derived from various methods and calculation models will be a key research direction moving forward. However, due to the limited number of tests conducted in this study, the relationship between structural parameters was not established. To reduce structural differences between samples, the MIP and N_2A detection processes could be integrated with XCT technology for *in-situ* pore structure detection during mercury or nitrogen loading, thereby improving both detection efficiency and accuracy. Building on this, the relationship between structure and macroscopic properties could be further explored by incorporating additional experimental samples.

4. Conclusions

Although the three studied methods, *i.e.*, XCT, N_2A and MIP, to analyze the wood structural features differ in their corresponding principle, they all effectively describe the structural differences among wood species at their dedicated detection range. While N_2A and XCT concentrate in the mesoporous (from *ca.* 1 nm to *ca.* 200 nm) and macroporous (from *ca.* 1 μm to *ca.* 300 μm) range, respectively, MIP covers both ranges (from *ca.* 1 nm to *ca.* 300 μm), showing a better picture of the pore distribution.

Based on theoretical analysis, the porosity measured by MIP is likely the closest to the true value, showing different pore size distributions in the meso-, macro- and large macroporous scales. The average porosity for the three species, *i.e.*, pine, birch and oak, was 0.648, 0.545, and 0.443, respectively, which is inversely proportional to the corresponding density. Due to limitations in the detection scale, the porosity measured by XCT is slightly lower than that of MIP. The N_2A method yields the highest porosity, which may be attributed to its detection principle. When ignoring the structural variability of the samples, the average pore diameter and PSD obtained by MIP and XCT methods fall in the same order of magnitude and range, which is not the case for N_2A. The fractal dimension values of the three wood species are quite similar for the three methods and range from 1.7 to 1.9.

It can be concluded that each method has its own advantages. Therefore, joint characterization using multiple methods should become the mainstream approach in the future. However, the pore structure parameters, especially those that describe the structural characteristics, need to be evaluated and analyzed using appropriate models. On this basis, efforts should be made to establish the internal relationships between structural parameters by collecting extensive data from various specimens.

CRediT authorship contribution statement

Zhipeng Zhu: Writing – original draft, Funding acquisition, Formal analysis, Data curation. **Fan Wu:** Data curation. **Xiaoxue Song:** Writing – review & editing, Funding acquisition. **Wanli Cheng:** Writing – review & editing. **Antoni Sanchez-Ferrer:** Writing – review & editing, Methodology, Conceptualization. **Jingyao Zhao:** Writing – review & editing, Methodology, Funding acquisition, Conceptualization.

Declaration of competing interest

The authors declare that they have no known competing financial interests or personal relationships that could have appeared to influence the work reported in this paper.

Acknowledgments

This work was supported by the National Natural Science Foundation of China (No. 32271786 and 32401501), the Fundamental Research Funds for the Central Universities (No. 2572023AW54), and National Undergraduate Training Programs for Innovations (No. 202510225086). Scientific Compass (www.shiyanjia.com) assisted with the the mercury intrusion porosimetry testing part of this work.

Data availability

Data will be made available on request.

References

Biziks, V., Van Acker, J., Militz, H., Grinins, J., Van den Bulcke, J., 2018. Density and density profile changes in birch and spruce caused by thermo-hydro treatment measured by X-ray computed tomography. Wood Sci. Technol. 53 (2), 491–504. https://doi.org/10.1007/s00226-018-1070-6.

Brodersen, C.R., Choat, B., Chatelet, D.S., Shackel, K.A., Matthews, M.A., McElrone, A.J., 2013. Xylem vessel relays contribute to radial connectivity in grapevine stems (*Vitis vinifera and V. arizonica; Vitaceae*). Am. J. Bot. 100 (2), 314–321. https://doi.org/10.3732/ajb.1100606.

Burridge, H.C., Pini, R., Shah, S.M.K., Reynolds, T.P.S., Wu, G., Shah, D.U., Scherman, O.A., Ramage, M.H., Linden, P.F., 2021. Identifying efficient transport pathways in early-wood timber: insights from 3D X-ray CT imaging of softwood in the presence of flow. Transport Porous Media 136 (3), 813–830. https://doi.org/10.1007/s11242-020-01540-8.

El Assaad, M., Colinart, T., Lecompte, T., 2023. Thermal conductivity assessment of moist building insulation material using a heat flow meter apparatus. Build. Environ. 234. https://doi.org/10.1016/j.buildenv.2023.110184.

Fang, C., Mariotti, N., Cloutier, A., Koubaa, A., Blanchet, P., 2011. Densification of wood veneers by compression combined with heat and steam. Eur. J. Wood Wood Prod. 70 (1–3), 155–163. https://doi.org/10.1007/s00107-011-0524-4.

He, S., Chen, Y., Wu, Z., 2020. Research progress on wood/bamboo microscopic fluid transportation. J. Fore. Eng. 2 (5), 12–19. https://doi.org/10.13360/j.issn.2096-1359.201906043.

Hu, M., Olsson, A., Hall, S., Seifert, T., 2022. Fibre directions at a branch-stem junction in Norway spruce: a microscale investigation using X-ray computed tomography. Wood Sci. Technol. 56 (1), 147–169. https://doi.org/10.1007/s00226-021-01353-y.

Huang, D., Wang, X., Li, X., Su, L., Tian, J., 2025. Advanced nuclear magnetic resonance technology analysis of hybrid fiber reinforced concrete for optimized pore structure and strength. Constr. Build. Mater. 467. https://doi.org/10.1016/j.conbuildmat.2025.140383.

Jang, E.S., Yuk, J.H., Kang, C.W., 2020. An experimental study on change of gas permeability depending on pore structures in three species (*Hinoki, Douglas fir, and Hemlock*) of softwood. J. Wood Sci. 66 (78), 1–12. https://doi.org/10.1186/s10086-020-01925-9.

Li, Z., Shen, X., Qi, Z., Hu, R., 2018. Study on the pore structure and fractal characteristics of marine and continental shale based on mercury porosimetry, N_2 adsorption and NMR methods. J. Nat. Gas Sci. Eng. 53, 12–21. https://doi.org/10.1016/j.jngse.2018.02.027.

Li, Y., Bi, J., Zhao, Y., Wang, C., Zhang, Y., Zhou, C., Ning, L., Deng, X., Zhou, Z., 2025. Study on the effect of pore structure characteristics on microbially strongly weathered phyllite under thermal fatigue. Constr. Build. Mater. 458. https://doi.org/10.1016/j.conbuildmat.2024.139533.

Li Jian, G.W., 2021. Research progress on wood biomimetic intelligent materials. Chinese J. Wood Sci. Technol. 35 (4), 1–14. https://doi.org/10.12326/j.2096-9694.2021051.

Michael, P., Niemz, P., 2011. Porosity and pore size distribution of different wood types as determined by mercury intrusion porosimetry. Eur. J. Wood Wood Prod. 69, 649–657. https://doi.org/10.1007/s00107-010-0504-0.

Mo, W., Kong, F., Chen, K., Li, B., 2022. Relationship between freeze-drying and supercritical drying of cellulosic fibers with different moisture contents based on pore and crystallinity measurements. Wood Sci. Technol. 56 (3), 867–882. https://doi.org/10.1007/s00226-022-01387-w.

Mohammadi, M., Shadizadeh, S.R., Manshad, A.K., Mohammadi, A.H., 2020. Experimental study of the relationship between porosity and surface area of carbonate reservoir rocks. J. Pet. Explor. Prod. Technol. 10, 1817–1834. https://doi.org/10.1007/s13202-020-00838-z.

Muthuraj, R., Lacoste, C., Lacroix, P., Bergeret, A., 2019. Sustainable thermal insulation biocomposites from rice husk, wheat husk, wood fibers and textile waste fibers: elaboration and performances evaluation. Ind. Crops Prod. 135, 238–245. https://doi.org/10.1016/j.indcrop.2019.04.053.

Papadopoulos, A.N., Bikiaris, D.N., Mitropoulos, A.C., Kyzas, G.Z., 2019. Nanomaterials and chemical modifications for enhanced key wood properties: a review. Nanomaterials 9 (4). https://doi.org/10.3390/nano9040607.

Portsmouth, R.L., Gladden, L.F., 1991. Determination of pore connectivity by mercury porosimetry. Chem. Eng. Sci. 46 (12), 3023–3036. https://doi.org/10.1016/0009-2509(91)85006-J.

Rajagopal, H., Khairuddin, A.S.M., Mokhtar, N., Ahmad, A., Yusof, R., 2019. Application of image quality assessment module to motion-blurred wood images for wood species identification system. Wood Sci. Technol. 53, 967–981. https://doi.org/10.1007/s00226-019-01110-2.

Razavifar, M., Mukhametdinova, A., Nikooee, E., Burukhin, A., Rezaei, A., Cheremisin, A., Riazi, M., 2021. Rock porous structure characterization: a critical assessment of various state-of-the-art techniques. Transport Porous Media 136 (2), 431–456. https://doi.org/10.1007/s11242-020-01518-6.

Redman, A.L., Bailleres, H., Turner, I., Perré, P., 2016. Characterisation of wood–water relationships and transverse anatomy and their relationship to drying degrade. Wood Sci. Technol. 50 (4), 739–757. https://doi.org/10.1007/s00226-016-0818-0.

Sánchez-Ferrer, A., Guerrero Parra, J., 2025. Exploring wood as a sustainable solution for water filtration: nanoparticle removal, size exclusion and molecular adsorption. Wood Sci. Technol. 59 (3). https://doi.org/10.1007/s00226-025-01645-7.

Sanchez-Ferrer, A., Böger, T., Engelhardt, M., Suh, F.T., Richter, K., 2023. Wood-water interactions of primers to enhance wood-polyurethane bonding performance. Wood Sci. Technol. 58 (1), 135–160. https://doi.org/10.1007/s00226-023-01508-z.

Taylor, A., Plank, B., Standfest, G., Petutschnigg, A., 2013. Beech wood shrinkage observed at the micro-scale by a time series of X-ray computed tomographs (μXCT). Holzforschung 67 (2), 201–205. https://doi.org/10.1515/hf-2012-0100.

Tibebu, D.T., Avramidis, S., Walters, C., 2023. Fractal dimension of wood cell wall pores from pore size distribution: insights from nitrogen gas adsorption analyzer. Wood Sci. Technol. 57 (3), 651–669. https://doi.org/10.1007/s00226-023-01472-8.

Trtik, P., Dual, J., Keunecke, D., Mannes, D., Niemz, P., Stahli, P., Kaestner, A., Groso, A., Stampanoni, M., 2007. 3D imaging of microstructure of spruce wood. J. Struct. Biol. 159 (1), 46–55. https://doi.org/10.1016/j.jsb.2007.02.003.

Wang, C., Biswas, S.K., Okubayashi, S., 2020. Polyethylenimine-Impregnated mesoporous delignified wood with high mechanical strength for CO_2/N_2 selective adsorption. ACS Appl. Nano Mater. 3 (6), 5499–5508. https://doi.org/10.1021/acsanm.0c00799.

Wanwan, Z., Rui, L., Yaoli, Z., 2022. Examination of pore structure in wood cell walls of poplar clone using nitrogen adsorption. J. Fore. Eng. 3 (7), 80–85. https://doi.org/10.13360/j.issn.2096-1359.202107043.

Wason, J.W., Brodersen, C.R., Huggett, B.A., 2019. The functional implications of tracheary connections across growth rings in four northern hardwood trees. Ann. Bot. 124 (2), 297–306. https://doi.org/10.1093/aob/mcz076.

Wildenschild, D., Sheppard, A.P., 2013. X-ray imaging and analysis techniques for quantifying pore-scale structure and processes in subsurface porous medium systems. Adv. Water Resour. 51, 217–246. https://doi.org/10.1016/j.advwatres.2012.07.018.

Xu, J., Zhao, D., Wang, S., Chen, X., Wu, X., Han, Z., Liu, Y., 2025. Quantitative analysis of pore structure's impact on early mechanical properties and durability of foam concrete: macroscopic and mesoscopic insights. Constr. Build. Mater. 459. https://doi.org/10.1016/j.conbuildmat.2024.139775.

Yin, J., Song, K., Lu, Y., Zhao, G., Yin, Y., 2015. Comparison of changes in micropores and mesopores in the wood cell walls of sapwood and heartwood. Wood Sci. Technol. 49 (5), 987–1001. https://doi.org/10.1007/s00226-015-0741-9.

Yin, J., Yuan, T., Lu, Y., Song, K., Li, H., Zhao, G., Yin, Y., 2017. Effect of compression combined with steam treatment on the porosity, chemical composition and cellulose crystalline structure of wood cell walls. Carbohydr. Polym. 155, 163–172. https://doi.org/10.1016/j.carbpol.2016.08.013.

Yu, Q., Dai, Z., Zhang, Z., Soltanian, M., Yin, S., 2019. Estimation of sandstone permeability with SEM images based on fractal theory. Transport Porous Media 126 (3), 701–712. https://doi.org/10.1007/s11242-018-1167-2.

Yuan, Y., Doonechaly, N., Rahman, S., 2016. An analytical model of apparent gas permeability for tight porous media. Transport Porous Media 111 (1), 193–214. https://doi.org/10.1007/s11242-015-0589-3.

Yun, M., Yu, B., Lu, J., Zheng, W., 2010. Fractal analysis of herschel-Bulkley fluid flow in porous media. Int. J. Heat Mass Tran. 53 (17–18), 3570–3574. https://doi.org/10.1016/j.ijheatmasstransfer.2010.04.020.

Zeng, L., Zhu, J., Zhao, Y., Wang, S., Huang, H., Zhang, J., Ye, J., 2023. Pore structure characteristics and permeability analysis of natural anhydrite with various water/anhydrite ratios based on mercury intrusion porosimetry. Constr. Build. Mater. 398. https://doi.org/10.1016/j.conbuildmat.2023.132422.

Zhang, Y., Wu, K., Yang, Z., Ye, G., 2022. A reappraisal of the ink-bottle effect and pore structure of cementitious materials using intrusion-extrusion cyclic mercury porosimetry. Cement Concr. Res. 161. https://doi.org/10.1016/j.cemconres.2022.106942.

Zhang, R., Zhang, M., Zhao, H., Wang, Y., Peng, Y., Ma, E., Cao, J., 2024. Revealing the behavior and mechanism of surfactant-assisted liquid permeability in poplar wood. Ind. Crops Prod. 209. https://doi.org/10.1016/j.indcrop.2023.117998.

Zhao, J., Yang, L., Cai, Y., 2020. Combining mercury intrusion porosimetry and fractal theory to determine the porous characteristics of wood. Wood Sci. Technol. 55 (1), 109–124. https://doi.org/10.1007/s00226-020-01243-9.

Zhao, J., Li, L., Lv, P., Sun, Z., Cai, Y., 2023. A comprehensive evaluation of axial gas permeability in wood using XCT imaging. Wood Sci. Technol. 57 (1), 33–50. https://doi.org/10.1007/s00226-022-01449-z.